Modeling the High Resolution X-ray Spectra from the Relativistic Jets of the X-ray Binary SS 433

by

Laura Ann Lopez

Submitted to the Department of Physics
in partial fulfillment of the requirements for the degree of

Bachelor of Science in Physics

at the

MASSACHUSETTS INSTITUTE OF TECHNOLOGY

June 2004

Author .....
Department of Physics
May 7, 2004

Certified by .....
Herman L. Marshall
Research Physicist
Thesis Supervisor

Certified by .....
Claude R. Canizares
Professor
Thesis Supervisor

Accepted by .....
David E. Pritchard
Physics Undergraduate Thesis Coordinator

Modeling the High Resolution X-ray Spectra from the Relativistic Jets of the X-ray Binary SS 433

by

Laura Ann Lopez

Submitted to the Department of Physics
on May 7, 2004, in partial fulfillment of the
requirements for the degree of
Bachelor of Science in Physics

Abstract

We test the physical model of the relativistic jets in the galactic X-ray binary SS 433 that was proposed by Marshall et al. 2002 (Paper I) using additional observations from the Chandra High Energy Transmission Grating Spectrometer. These observations sample two new orbital/precessional phase combinations. In the observation near orbital phase zero, the H- and He-like Fe lines from both receding and approaching jets are comparably strong and unocculted while the He-like Si line of the receding jet is significantly weaker than that of the approaching jet. This observation indicates the cooler parts of the jet are eclipsed by the companion. The spectrum from this observation has broader emission lines than obtained in Paper I; the opening angle of the jet is $2.70° \pm 0.32°$, double the previous Paper I result of $1.22° \pm 0.06°$. This result indicates the jet base may be five times smaller than the previous observation, with a jet launch radius of 21.3±3.1 Schwarzschild radii. Using the optical results presented by Gies et al. 2002, along with the length of the unobscured portion of the receding jet determined using a physical model of the X-ray spectrum, we calculate the radius of the companion to be $9.1 \pm 1.0\ R_{sun}$, about one third of the Roche lobe radius. For a main sequence star, this result corresponds to a companion mass of $29 \pm 7\ M_{sun}$, giving a primary source mass of $16 \pm 4\ M_{sun}$. This calculation indicates the compact object is a black hole, and accretion occurs through a wind process.

Thesis Supervisor: Herman L. Marshall
Title: Research Physicist

Thesis Supervisor: Claude R. Canizares
Title: Professor

Acknowledgments

I greatfully acknowledge my advisors, Dr. Herman L. Marshall and Professor Claude R. Canizares. They have provided invaluable guidance throughout my time working with them, and they contributed tremendously to this thesis. I also thank Dr. Nobert S. Schulz and Ms. Julie F. Kane who contributed to the science written in this paper.

Contents

List of Figures

List of Tables

Chapter 1

Introduction

In 1962, a team of scientists detected the first X-ray sources outside the solar system [1]. The researchers launched detectors aboard an Aerobee rocket, and they promptly discovered Scorpius X-1, the brightest soft X-ray source in the sky. Over forty years later, over one-hundred thousand X-ray sources have been identified. The field of X-ray astronomy has rapidly developed in the last few decades, largely because of advances in X-ray telescopes and detectors. This relatively young science has contributed greatly to scientists' understanding of stellar births and deaths, the formation and dynamics of galaxies, and the origin and evolution of the universe. In this chapter, I will highlight major X-ray astronomy developments and missions in the last four decades as back drop to the capabilities and science of the *Chandra* X-ray Observatory. For brevity, only prominent missions or ones mentioned in this thesis are discussed. For a comprehensive review of the field, see [2] and [3].

1.1 An Overview of Past X-ray Missions

Table 1.1 summarizes past X-ray missions in chronological order. The early discoveries by [1] and others catalyzed a strong push toward X-ray astronomy. In December 1970, the first satellite dedicated to X-ray observations *Uhuru* was launched by NASA off the coast of Kenya. Using a sensitive proportional counter to locate sources in the 2 to 20 keV range, it conducted a large sky survey and identified many new X-ray

Satellite	Launch	Type	Energy Range (keV)
Vela 5A,B	May 69	Scanning, small SC	3-12
Uhuru	Dec 70	Scanning, large PC	2-10
OSO-7	Sep 71	Scanning, PC	1-40
Copernicus	Aug 72	Pointed, small concentrator	0.2-10, 0.2-0.6
ANS	Aug 74	Pointed, PC, Bragg crystal	2-40
Ariel-V	Oct 74	Scanning, pointed, ASM, large PC	2-10
SAS-3	May 75	Scanning, RMC, large PC	1.5-10
HEAO-1	Aug 77	Scanning, very large PC, SC	1-20
Einstein	Nov 78	Pointed, telescope, PC, HRI, Si detector	0.2-4
Hakucho	Feb 79	Scanning, RMC, large PC	0.1-2, 2-20
Tenma	Feb 83	Scanning, GSPC, ASM	2-10
EXOSAT	May 83	Pointed, small telescope, large PC	0.05-2.0, 1.5-10
Ginga	Feb 87	Pointed, large PC	1.5-30
ROSAT	June 90	Scanning, pointed, telescope, PC, HRI	0.1-2.5
ASCA	Feb 93	Pointed, telescope, CCD, GSPC	0.4-12
RXTE	Dec 95	Pointed, large PC, large SC, ASM	2-50, 15-200
BeppoSAX	Apr 96	Pointed, GSPC, SC, WFC	0.1-300
Chandra	Jul 99	Pointed, telescope, CCD, HRI, gratings	0.1-10
XMM-Newton	Dec 99	Pointed, telescope, CCD, HRI, gratings	0.1-15

Table 1.1: Some X-ray Astronomy Missions (adapted from [7]) Key: ASM = all-sky monitor; CCD = charged coupled detector; GSPC = gas scintillation proportional counter; HRI = high resolution, channel plate detector; PC = proportional counter; RMC = rotating modulation collimator; SC = scintillation counter; WFC = wide-field camera

sources [4]. Additionally, *Uhuru* showed X-ray stars are neutron stars or black holes accreting material from donor stars in binary systems (see [5] or [6], for example). Known as X-ray binaries, these sources will be discussed in detail in Chapter 2.

NASA continued its X-ray astronomy efforts with the launch of the High-Energy Astronomy Observatories in 1977. The first of these missions, *HEAO-1*, surveyed the sky over the range 0.2 keV to 10 MeV. *HEAO-1* was the first comprehensive catalog of X-ray sources, and many objects were classified based on their X-ray source positions. *HEAO-1* monitored variability in a variety of systems, from active-galactic nuclei to X-ray binaries.

The second *HEAO* mission, named the Einstein Observatory, was the first large X-ray telescope with mirrors to facilitate X-ray imaging. Einstein boasted resolution of a

few arcseconds, a field-of-view on the order of tens of arcminutes, and sensitivity vastly better than any previous missions. In conjunction with a high-resolution imager, Einstein contained an objective grating spectrometer, an instrument that facilitated the first high resolution X-ray spectroscopy studies of high-energy sources.

In 1983, the European Space Agency launched its own X-ray observatory, *EXOSAT*, with grazing incidence imaging telescopes as well as low-energy transmission gratings for spectroscopy work. Spanning an energy range of 0.05 to 50 keV, *EXOSAT* was the first observatory to detect the Fe-K fluoresence line from galactic and extragalactic X-ray sources. *EXOSAT* also discovered quasi-periodic oscillations from neutron stars and black holes [8] as well as conducted a comprehensive study of variability in galactic and extragalactic objects. At this point, over one-hundred thousand X-ray sources had been discovered.

Japan also became heavily involved in the field of X-ray astronomy and organized four missions. The third of these, the *Ginga* satellite, was an observatory with a large area proportional counter as its primary instrument. Ranging from 1 to 500 keV, *Ginga* discovered transient black hole candidates and examined their spectral evolution (see [9], for example). *Ginga* detected intense iron emission from the galactic center as well as cyclotron features in X-ray pulsars.

In 1990, Germany launched the Roentgen Satellite (or ROSAT) that operated for almost nine years. For the first six months, it conducted a large all-sky survey with about 1000 times better resolution than that of *Uhuru*. *ROSAT*'s scientific return was extensive, from resolving 70% of the soft X-ray background to detecting the first radiation from the surface of a neutron star. *ROSAT* identified 25,000 new X-ray sources and provided much of the foundation for present-day X-ray surveys.

Japan continued its X-ray astronomy endeavors in 1993 with the Advanced Satellite for Cosmology and Astrophysics (*ASCA*). With low resolution mirrors and the first large CCD detectors, *ASCA* was especially designed for resolved spectral studies in the 0.4 to 10 keV range. Detections of the broad Fe line in active-galactic nuclei were the first evidence of gravitational redshift around black holes. Additionally, *ASCA* obtained the most resolved spectra of its time from X-ray binaries and other

high-energy sources.

1.2 The Era of Chandra

In July 1999, NASA's *Chandra* X-ray Observatory was launched and deployed by the Space Shuttle Columbia. With approximately fifty times better imaging resolution than *ROSAT* and one-hundred times better spectral resolution than *ASCA*, *Chandra* is one of the most sophisticated X-ray observatories built to date. The observatory has a highly elliptical orbit, taking the spacecraft from within ten-thousand miles of the Earth to nearly a third of Earth-Moon distance. Above the charged particles of the Earth's atmosphere for nearly 85% of its orbit, Chandra has more useful observing time than most other satellites.

Chandra has three primary components, as shown in Figure 1-1: the X-ray telescope, the science instruments, and the space craft. The telescope is comprised of four pairs of mirrors that direct incoming X-rays toward a focal point approximately thirty feet away. There, focal plane science instruments capture the images formed by the mirrors and reveal information about the incoming X-rays, such as their position and energy.

1.2.1 Imaging Instruments

Chandra has two instruments to capture the images formed by the mirrors: the High Resolution Camera (HRC) and the Advanced CCD Imaging Spectrometer (ACIS). Matched with the *Chandra* mirrors, the HRC can take images that reveal details as small as one-half an arcsecond. The HRC has two Micro-Channel Plates (MCP) comprised of 69 million tiny lead-oxide tubes. These tubes have a special coating that causes the release of electons when struck by X-rays. Electrons are accelerated down the tubes by a voltage supply, and a crossed-wire grid detects the resulting electronic signal facilitating determination of the X-ray's position. The high precision of the HRC make it especially useful for imaging very distant and faint X-ray sources.

The ACIS instrument is an array of charged-coupled devices that simultaneously

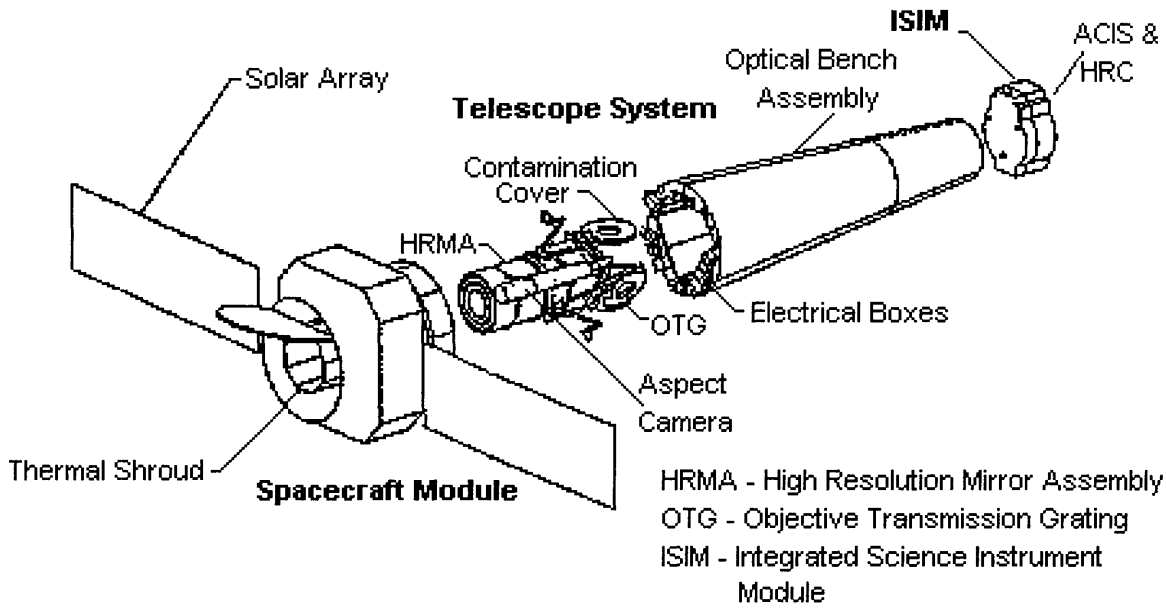

Figure 1-1: Diagram of the major components of the Chandra X-ray Observatory.

produce X-ray images and measure the energy of each incoming X-ray. Thus, the ACIS can produce pictures of objects using X-rays produced by single chemical elements. Many scientists use this instrument to study temperature and chemical composition variations across clouds left by supernovae or hot gas in intergalactic space.

1.2.2 High Resolution Spectrometers

Two Chandra instruments are dedicated to high resolution X-ray spectroscopy: the High-Energy Transmission Grating Spectrometer (HETGS) and the Low-Energy Transmission Grating Spectrometer. The gratings diffract X-rays, changing their direction depending uniquely on the X-ray energy. Then, either HRC or ACIS detects the location of the diffracted X-ray, facilitating determination of its energy. The gratings can measure energy to an accuracy of up to one part in a thousand. In conjunction with Chandra's sharp mirror focus and exceptional detector resolution, the gratings can be used to distinguish individual X-ray lines in complex spectra. Analysis of these data can reveal the temperature, ionization, and chemical composition of exotic

astrophysical systems.

This thesis will focus on analysis of data from the *Chandra* HETGS. These gratings span an energy range of 0.4 to 10 keV. An important feature of the HETGS is that spectra are obtained independently and simultaneously from the High-Energy Gratings (HEG) and the Medium-Energy Gratings (MEG). The HEG have twice the spectral resolution and larger effective area above 4 keV than the MEG. In contrast, the MEG have an extended bandpass and more effective area for detecting low-energy emission lines (such as iron).

Chapter 2

X-ray Binaries

2.1 General Properties

After its discovery as the first observed non-solar X-ray point source, Scorpius X-1 was quickly classified as an X-ray binary system [10, 11, 12]. An X-ray binary consists of either a neutron star or a black hole accreting material from a companion star. X-ray binaries are the brightest class of X-ray sources in the sky, and more than 200 have been identified from X-ray surveys and optical identification programs.

X-ray binaries exhibit a wide range of characteristics, such as orbital periods from 11 minutes to 1 year and donor star masses from 0.01 to 30 solar masses. Astronomers classify X-ray binaries into two groups: low-mass X-ray binaries (systems with a stellar companion mass $<$ 1 solar mass) and high-mass X-ray binaries (sources with donor mass $>$ 8 solar masses). In LMXBs, the donor is later than type A, and mass transfer only occurs if the star fills its critical gravitational potential lobe, the Roche lobe. The donor is typically not detected at optical wavelengths, and the orbital periods are quite short at 1 day. In high-mass X-ray binaries (HMXBs), the donor is an O or B star with a substantial stellar wind that removes 10^{-6} to 10^{-10} solar masses per year. HMXBs typically have orbital periods of several tens of days.

2.2 The X-ray Binary SS 433

The galactic X-ray binary SS 433 has been the subject of intense study since it was catalogued as an emission-line object with strong Hα [13]. Located in the constellation Aquila, it is a relatively bright optical source with a V-magnitude of 14.2. Consequently, small instruments can detect the many features of this system, and extensive work has been conducted to understand its nature and history.

The first moderate-resolution spectral data revealed a complex system, with very strong Balmer and He I lines as well as a prominant broad emission features. The latter emissions were promptly attributed to Doppler-shifted Balmer and He I lines from two sources, one at a consistently high redshift and another at a large blueshift: maximum redshift is about 0.15 and maximum blueshift is around -0.08. The features changed wavelength and drifted through the spectrum with a periodic timescale of approximately 164 days. A "kinematic model" [14, 15, 16] predicted this behavior by attributing the "moving" emission lines to two identical, oppositely-directed jets emerging from a compact object at a constant velocity of .2602c. These jets precess in a 20° half-angle over a 164.25-day period, and the central axis of rotation is inclined 78.83° to the line of sight [17].

As a requirement for a source of material in the jets, researchers predicted SS 433 was a close binary system comprised of a compact object and a large donor star. This hypothesis was confirmed when a 13-day periodicity in the radial velocity of the "stationary" emission lines was discovered [18, 19]. These features originate in or near a hot, thick accretion disk that dominates the optical flux observed from the system. The strong disk spectrum obscures scientists' view of the orbitting companion, precluding detection of absorption features from the star's atmosphere that could identify its nature. Recently, scientists aimed to ameliorate this dilemma by observing the system while the donor during primary eclipse, when it blocks emission from the disk [20, 21, 22]. These studies find evidence of a weak absorption spectrum resembling that of an evolved A star. More optical work is necessary to obtain more resolved spectra and to confirm these results.

SS 433 has radio jets which display an oscillatory pattern as a result of material flowing hellically along ballistic trajectories [23]. Using observations with the Very-Long Baseline Interferometer observations, the kinematic model was confirmed and derived a distance estimate to the system: 4.85±0.2 kpc [24]. The radio jets extend from the milliarcsecond scale to several arcseconds, corresponding to a range of 10^{15-17} cm from the center of the compact object. The optical emission lines originate in a smaller region, $< 3 \times 10^{15}$ cm across, based on light travel time arguments [25]. Large scale X-ray emission is also coincident with the radio and optical and extends to approximately 1.5×10^{20} cm [26].

Initial *HEAO-1* observations demonstrated SS 433 as an X-ray source [27] and spectra were modelled as thermal bremsstrahlung with $kT = 14.3$ keV and emission from Fe-K near 7 keV. *Ginga* analysis placed kT around 30 keV [28], whereas the ratio of Fe XXV and Fe XXVI line fluxes from *ASCA* indicated a value of 20 keV [29]. The X-ray emission was modeled as originating at the jet bases and expanding adiabatically ([28] and [29]). As the jets travels outward, they cool until kT drops to 100 eV and become thermally unstable. Additionally, faint Fe XXV in the redward jet seemed to indicate that the redward jet was obscured by neutral disk material [29]. Although the *ASCA* spectra detected emission lines that were previously unobserved, the lines were unresolved and difficult to identify below 2 keV.

Despite these findings, many outstanding questions remain about SS 433: what are the masses and nature of the donor and collapsed stars? how and where do the jets form? how has this unusual binary evolved? In this thesis, we address some of these mysteries with new observations of the SS 433 system using the *Chandra* HETGS. We test the physical model of the jets proposed from a first observation [30] (hereafter, Paper I). The first observation aimed to resolve the X-ray lines, to detect fainter lines than previously observed, and to measure lower energy lines that could not be readily detected in the *ASCA* observations. This HETGS observation showed many emission lines, as previously known from *ASCA* observations [31]. In Paper I, the X-ray spectrum was dominated by thermal emission from the jets. Additionally, the electron density of the jet was estimated to be 10^{14} cm^3 using the Si XIII triplet,

providing an estimate for the size of the jet.

2.3 HETGS Observations of SS 433

In this first HETGS observation, blue-shifted lines dominated the spectrum and the red-shifted lines were all relatively weak by comparison, so most work focused on modelling the blue jet. The jet Doppler shifts were determined very accurately due to the small scatter of the individual lines and the narrowness of their profiles, indicating that all line-emitting gas flows at the same speed. The jet bulk velocity was βc, where β=0.2699 $\pm$ 0.0007. This jet velocity is larger than the velocity inferred from optical emission lines by 2920 $\pm$ 440 km s^{-1}. Gaussian fits to the emission lines were all consistent with the same Doppler broadening: 1700 $\pm$ 80 km s^{-1} (FWHM). Relating this broadening to the maximum velocity due to beam divergence, the opening angle of the jet was determined to be 1.23° $\pm$ 0.06°.

The new observations presented in this thesis were taken at two different combinations of precessional and orbital phases, offering different views of the jets. In particular, one observation was taken during eclipse. The goal of the studies was to determine which parts of the jets were blocked from view. Using optical spectroscopy results [20], along with the length of the jets determined from physical modeling of the X-ray spectrum, data were utilized to measure the size and mass of the companion. This result set a restriction on the mass of the compact object and ultimately support the hypothesis that the primary source is a black hole.

Previous X-ray observations of the SS 433 system during eclipse [28, 32] have not provided good detection of emission lines from the receding jet. This result has led some to believe the entire inner region of the jets was eclipsed. However, our spectrum from this observation shows numerous emission lines from the receding jet. Particularly, the presence of strong, highly-ionized Fe lines indicate only the low-energy portion of this jet was eclipsed.

Chapter 3

A Second HETGS Observation

SS 433 was observed a second time with the HETGS on 21 November 2000 for 24 ks. Based on the precession ephemeris by [17] and updated by [21], the angle of the jet to the line of sight during this observation was $\alpha = 96.0°$. At this phase, the typically blueward jet was temporarily pionted farther from the line of sight than the redward jet. From the binary ephemeris [33], the binary phase range was 0.68 to 0.70.

3.1 Imaging

The zeroth-order image from this observation, shown in Figure 3-1, is distincly elongated in the east-west direction. The extended X-ray emission was first reported in Paper I. This result is consistent with [34] who found evidence for outflowing hot plasma in the extended X-ray emission, indicating material is reheating very far from the compact object and the emission region is a factor of 10^4 larger than the area producing the bulk of the spectrum. The excess emission in the east-west direction is associated with the arcsecond-scale radio jet as observed by [23] using the VLBI.

Based on dispersion spectra (because the point source is somewhat piled up, as in Paper I), the X-ray flux from SS 433 increased by about 15% on a time scale of 10,000 seconds.

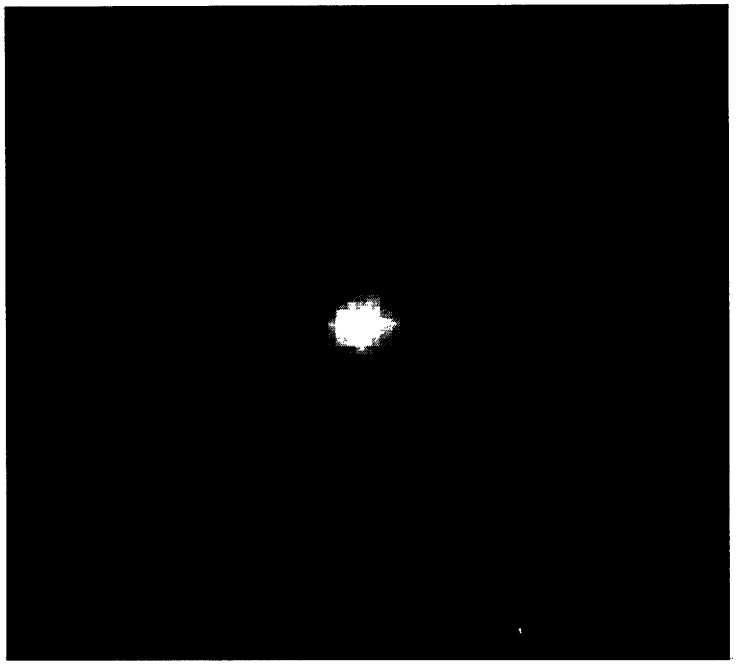

Figure 3-1: Image of SS 433 from the zeroth order of the *Chandra* HETGS. The image is extended along the east-west direction on a scale of 2-5″ as discovered in Paper I. The extent is comparable to that observed in the radio band by [23]. During this observation, the blueward jet precessed and pointed away from the observer, making it more redshifted than the redward jet.

3.2 Spectra

As in Paper I, the spectral data were reduced starting from level 1 data provided by the *Chandra* X-ray Center (CXC) using IDL custom processing scripts. The spectra from this observation is shown in Figure 3-2. The jet emission lines in the November 2001 observation are practically undetectable. Explanations for the line disappearance will be explored later in this thesis. However, this observation will not be analyzed further.

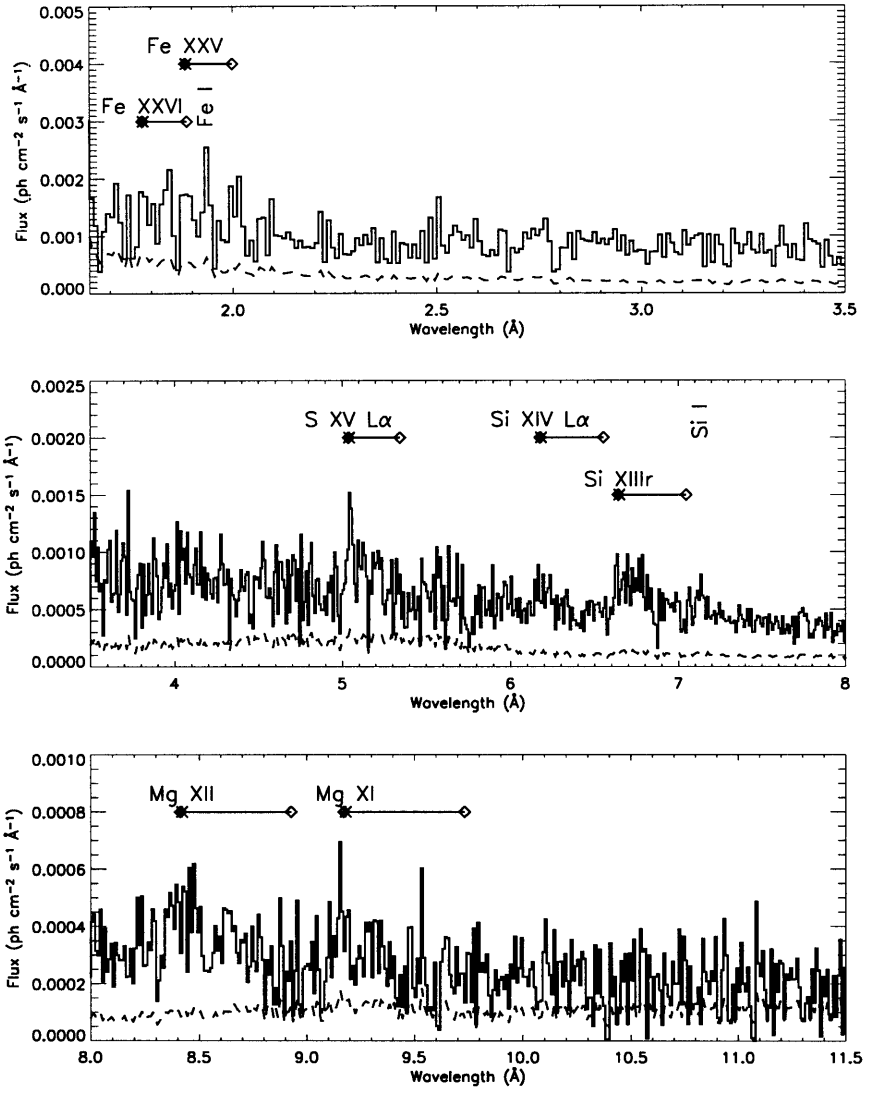

Figure 3-2: The X-ray spectrum of SS 433 observed with the *Chandra* HETGS in November 2001. The HEG and MEG data were combined at the resolution of the MEG spectrum. Possible line identifications are shown. Horizontal lines connect the locations of blue- and red-shifted lines (diamonds) to the rest wavelengths (asterisks). The dashed line gives the statistical uncertainties. Emission lines are resolved and their strengths indicate the plasma is collisionally dominated. Lines were extremely weak during this observation in both the red jet ($z = 0.070$) and blue jet ($z = -0.001$). The overall flux level is very low compared to the observation reported in Paper I and the March 2002 observation (Figure 4-2)

Chapter 4

A Third HETGS Observation During Eclipse

SS 433 was observed a third time with the HETGS on 16 March 2001 for 24 ks. The spectra were taken during eclipse when the companion blocked part of the X-ray continuum. Based on the precession ephemeris by [17] and updated by [21], the angle of the jet to the line of sight during this observation was $\alpha = 80.0°$. From the precession and binary ephemeris by [33], the binary phase range was 0.96 to 0.98.

4.1 Imaging

The zeroth-order image from this observation is shown in Figure 4-1. As in Figure 3-1, the image is elongated in the east-west direction. Based on the dispersed spectra, the X-ray flux was constant over the whole 24 ks observation.

4.2 Spectra

As with the second observation, the spectral data were reduced starting from level 1 data provided by the *Chandra* X-ray Center using IDL custom processing scripts. The spectra from this observation are shown in Figure 4-2.

Line fluxes for the March 2001 observation are given in Tables 4.1 to 4.3. A

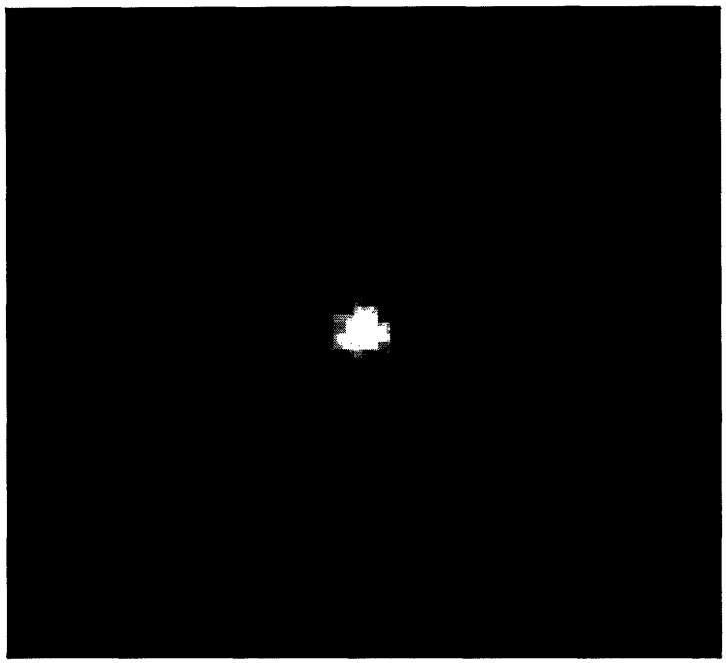

Figure 4-1: As in Figure 3-1, image of SS 433 from the zeroth order of the *Chandra* HETGS. Possible N-S structure from the first observation was not confirmed in the later observations. Note that the point source is still very bright during eclipse, indicating that the innermost, hottest regions of the jets are not occulted.

λ_{rest} (Å)	λ_{obs} (Å)	z	Flux (10^{-6} ph cm^{-2} s^{-1})	Identification
1.780	1.804 ± 0.004	0.0133 ± 0.0020	116. ± 25.	Fe XXVI Lyα[a]
1.855	1.881 ± 0.009	0.0144 ± 0.0049	593. ± 37.	Fe XXV 1s2p-1s^2 a
3.020	3.061 ± 0.009	0.0136 ± 0.0029	33. ± 10.	Ca XX Lyα
3.186	3.207 ± 0.007	0.0066 ± 0.0021	46. ± 10.	Ca XIX 1s2p-1s^2 b
3.952	4.004 ± 0.007	0.0130 ± 0.0016	31. ± 10.	Ar XVII 1s2p-1s^2
3.991	4.047 ± 0.005	0.0140 ± 0.0014	105. ± 16.	S XVI Lyβ
4.729	4.788 ± 0.005	0.0124 ± 0.0010	88. ± 14.	S XVI Lyα
5.055	5.128 ± 0.006	0.0143 ± 0.0012	88. ± 13.	S XV 1s2p-1s^2
5.217	5.262 ± 0.007	0.0085 ± 0.0013	53. ± 12.	Si XIV Lyβ
6.141	6.249 ± 0.002	0.0108 ± 0.0003	142. ± 8.	Si XIV Lyα
6.675	6.730 ± 0.003	0.0083 ± 0.0004	88. ± 7.	Si XIII 1s2p-1s^2
8.310	8.379 ± 0.011	0.0083 ± 0.0014	22. ± 5.	Fe XIII/XXIV
8.421	8.493 ± 0.005	0.0085 ± 0.0006	61. ± 6.	Mg XII Lyα c
9.103	9.166 ± 0.010	0.0071 ± 0.0011	25. ± 7.	Ne X RRC
10.636	10.742 ± 0.013	0.0100 ± 0.0012	31. ± 6.	Fe XXIV

Table 4.1: Blue Jet Line Fluxes.

λ_{rest} (Å)	λ_{obs} (Å)	z	Flux (10^{-6} ph cm^{-2} s^{-1})	Identification
1.937	1.942 ± 0.004	0.0025 ± 0.0018	100. ± 21.	Fe I
7.128	7.131 ± 0.006	0.0004 ± 0.0008	14. ± 3.	Si I - Si VII

Table 4.2: Rest Frame Line Fluxes. These emission features are discussed in detail in Section 6.3.

similar methodology from Paper I was utilized to fit the lines: lines were fitted to the MEG and HEG data jointly in five wavelength ranges after subtracting a polynomial fit to the continuum. Gaussian widths are given in Table 4.4. Only statistical errors are quoted; systematic uncertainties other than possible line misidentifications are expected to be smaller than 10%. The line widths are approximately double those found from the first observation.

The spectra are shown in Figures 4-2 to 4-5. Figure 4-2 shows the flux corrected spectrum, combining the MEG and HEG data with statistical weighting. Similar to the first observation, many broad emission lines and a significant continuum are prevalent. Unlike the Paper I spectrum, the new data shows roughly the same emission

λ_{rest} (Å)	λ_{obs} (Å)	z	Flux (10^{-6} ph cm^{-2} s^{-1})	Identification
1.780	1.881 ± 0.001	0.0570 ± 0.0005	593. ± 37.	Fe XXVI Lyα a
1.855	1.973 ± 0.001	0.0641 ± 0.0006	348. ± 28.	Fe XXV 1s2p-1s^2 a
3.020	3.207 ± 0.007	0.0619 ± 0.0022	46. ± 10.	Ca XX Lyα b
3.186	3.382 ± 0.007	0.0614 ± 0.0021	41. ± 10.	Ca XIX 1s2p-1s^2
3.952	4.213 ± 0.008	0.0659 ± 0.0020	57. ± 11.	Ar XVII 1s2p-1s^2
3.991	4.213 ± 0.008	0.0557 ± 0.0020	57. ± 11.	S XVI Lyβ
4.729	5.033 ± 0.004	0.0643 ± 0.0008	113. ± 13.	S XVI Lyα
5.055	5.354 ± 0.013	0.0591 ± 0.0026	37. ± 12.	S XV 1s2p-1s^2
6.182	6.561 ± 0.004	0.0612 ± 0.0006	58. ± 6.	Si XIV Lyα
6.675	7.057 ± 0.006	0.0573 ± 0.0010	32. ± 5.	Si XIII 1s2p-1s^2
7.989	8.493 ± 0.005	0.0630 ± 0.0007	61. ± 6.	Fe XXIV c
9.103	9.637 ± 0.013	0.0588 ± 0.0014	25. ± 6.	Ne X RRC

Table 4.3: Red Jet Line Fluxes.

Wavelength Range (Å)	v (km s^{-1})
1.5 – 2.5	1492 ± 109
2.5 – 4.0	1595 ± 352
4.0 – 5.5	1629 ± 195
5.5 – 7.5	1190 ± 60
7.5 – 11.5	1246 ± 120

Table 4.4: Velocity wdiths (σ) of Gaussian line profiles at different wavelengths.

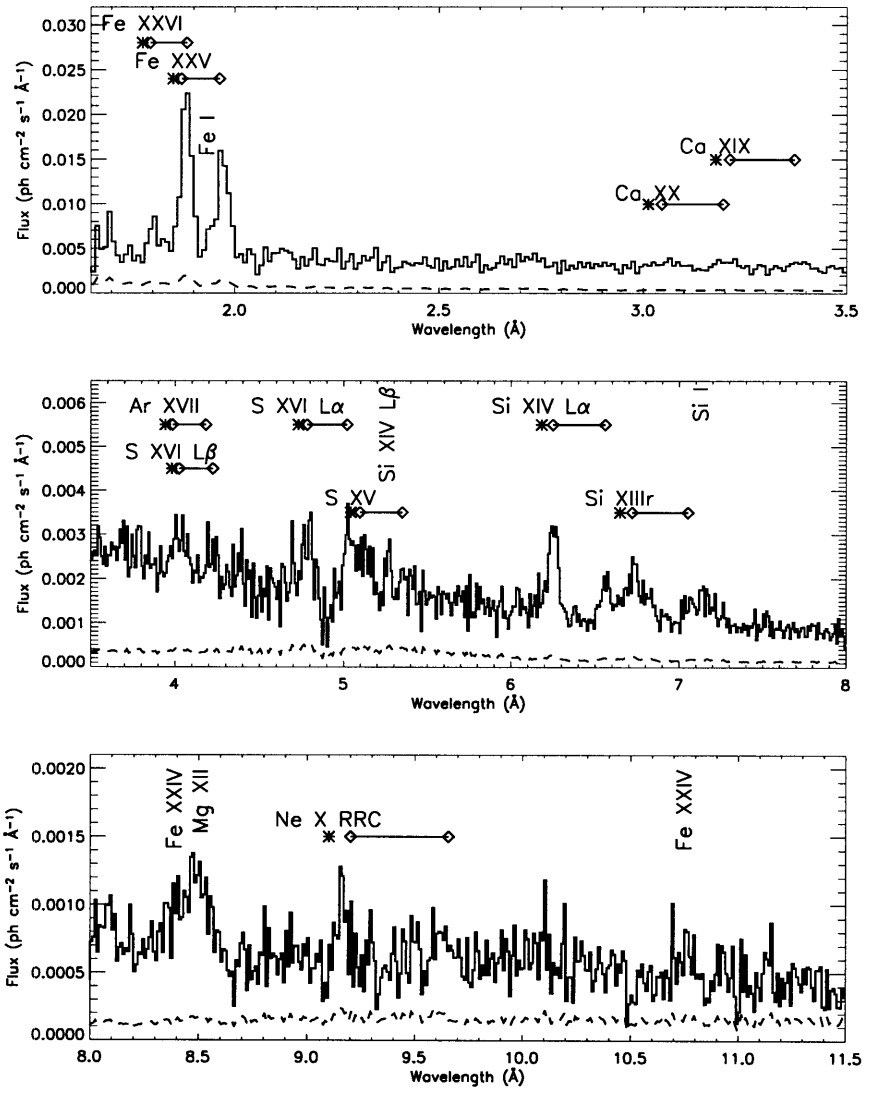

Figure 4-2: The X-ray spectrum of SS 433 observed with the *Chandra* HETGS in March 2002, as shown in Figure 3-2. Unlike the second observation, many prominent emission lines were observed. These lines are resolved, and their strengths indicate the plasma is collisionally dominated. The Fe XXV line from the blueward jet is confused with the Fe XXVI line of the receding jet. The Ne X radiative recombination continuum (RRC) feature is observed in both jets.

lines in the blue and red jets.

For each line, the ID was determined based on the expected shifts of the blue and red jets from the kinematic model and the measured redshift. For the precession phase of our observation, the predicted blue- and red-shifts were 0.011 and 0.063, respectively, using the equation and parameters in Table 1 of [17]. Wavelengths of line blends were obtained using the Astrophysical Plasma Emission Database (APED)[1] and were weighted by the relative fluxes of each component based on the models from Section 5. Analysis of the S XV and Si XIII triplets was replicated for this observation. Precise redshifts for these profiles were determined by fitting these blends with several variable-width Gaussian components and with fixed rest wavelength values given by APED, as implemented in the Interactive Spectral Identification System, ISIS[2]. The Si XIII line was used to determine the density in the jet. Unlike in Paper I, the red and blue jet lines were prominent enough to facilitate accurate measurement of the redshift for both jets. Two lines were not assigned to either the red or blue jets: a neutral Fe-K line and a Si I-K line, both at rest in the observed frame.

4.3 Line Widths and Positions

Table 4.1 shows that the Doppler shifts of the lines in the blue jet system are consistent with a single velocity to within the uncertainties, as are those in the red jet system. The few deviations are not likely indicative of intrinsic variations but are mostly due to blends of blue jet lines. Furthermore, all deviations are substantially smaller than the observed line widths, which are on the order of $\delta z = 0.006$ (FWHM). The Doppler shift of the blue jet was determined to be $z_b = 0.0111 \pm 0.0001$ during this observation (as opposed to the $z_b = -0.0779 \pm 0.0001$ from the previous observation). For the red jet, the unblended lines give $.0610 \pm 0.0001$ (compared to the $z_r = 0.1550 \pm 0.0004$ reported in Paper I).

As in Paper I, we assume the system is comprised of two perfectly opposed jets

[1] See `http://cxc.harvard.edu/atomdb/` for more information about APED.
[2] See `http://space.mit.edu/CXC/ISIS` for more information about ISIS.

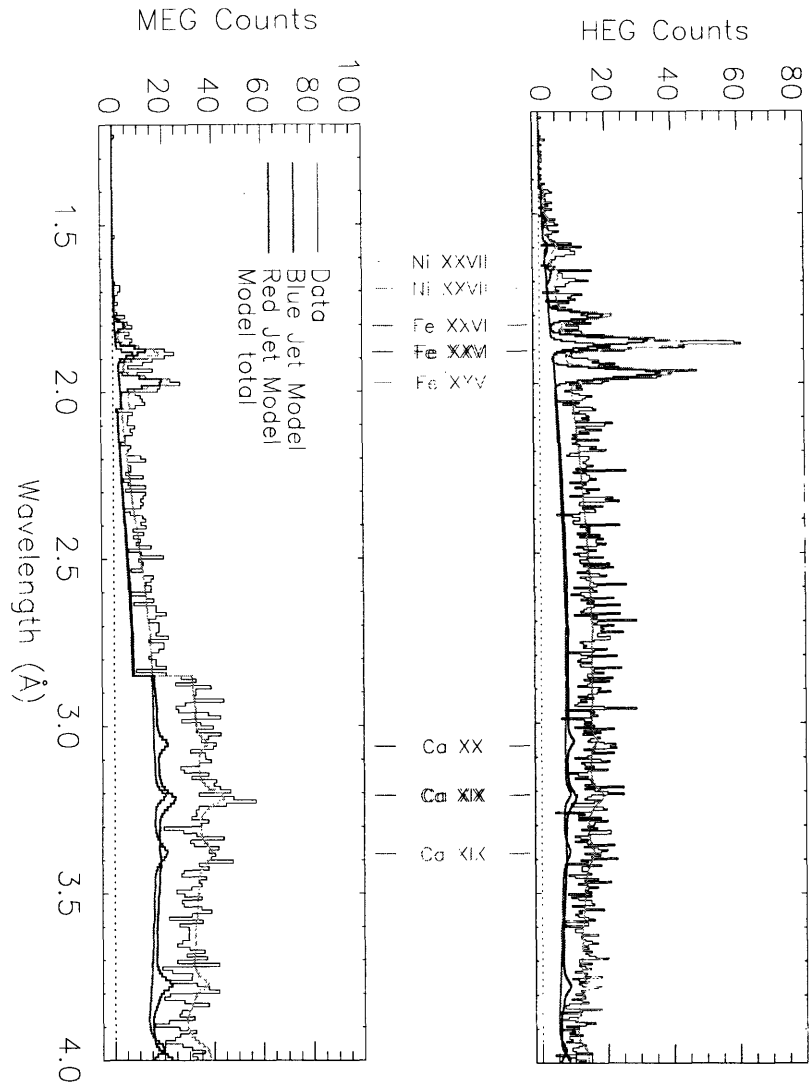

Figure 4-3: The 1.2-4.0 Å portions of the HEG and MEG spectra of SS 433 observed with the *Chandra* HETGS, compared to models of the spectra of the blue and red jets. The sum of the red and the blue spectra give the green curve. Line identifications are shown and measurements are given in Tables 4.1 to 4.3. The continuum is dominated by thermal bremsstrahlung emission. The edge in the spectrum at 2.8 Å is the result of excising data near a detector chip gap. In comparison to the first observation, the emission lines are more redshifted. The Fe I line, at rest in the observed frame, is in the same location. The blue and red jet Fe XXV and Fe XXVI lines are of nearly equal strength in the model, indicating that the hottest portions of the jets are not blocked by the companion during eclipse.

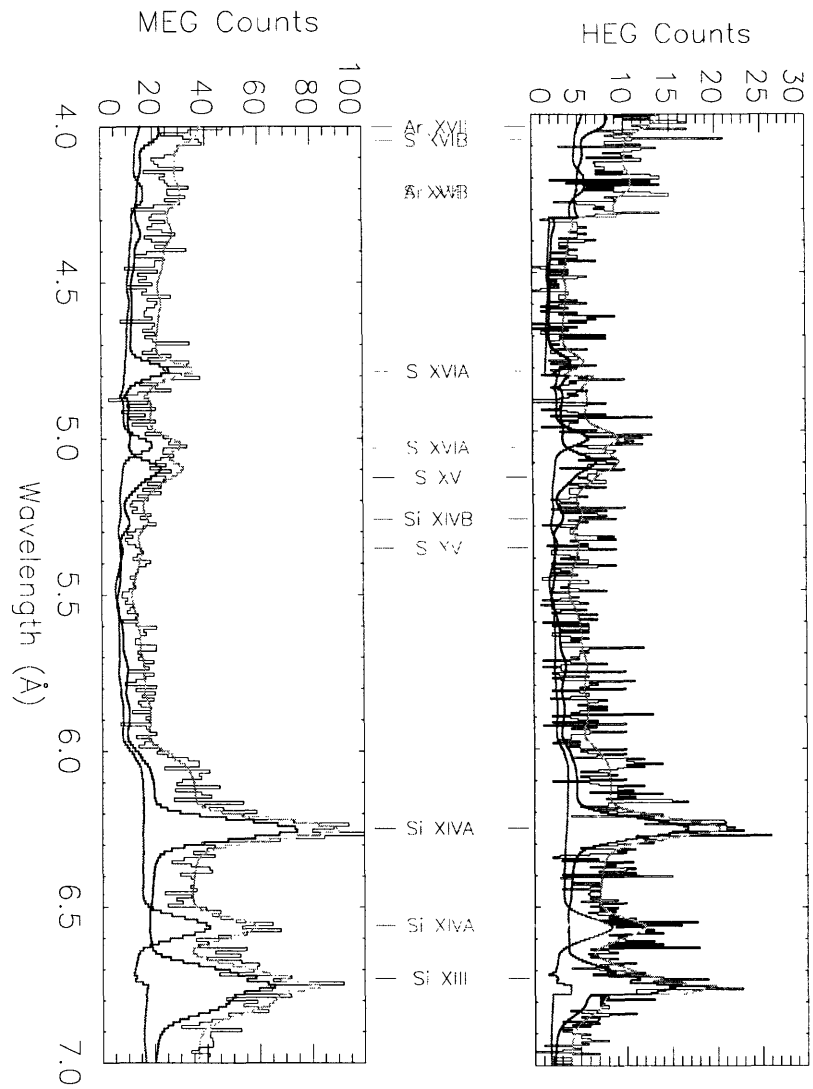

Figure 4-4: Same as Figure 4-3 except for the 4.0-7.0 Å region. Unlike the first observation, the red jet is still strong in this portion of the spectrum. The overall model continuum is slightly higher than the data in the 4-6 Å range, but the Si XIV and Si XIII lines are well fit. Because the model includes the instrumental response, there is a steep rise near 6.1 Å that results from the mirror Ir-M edge.

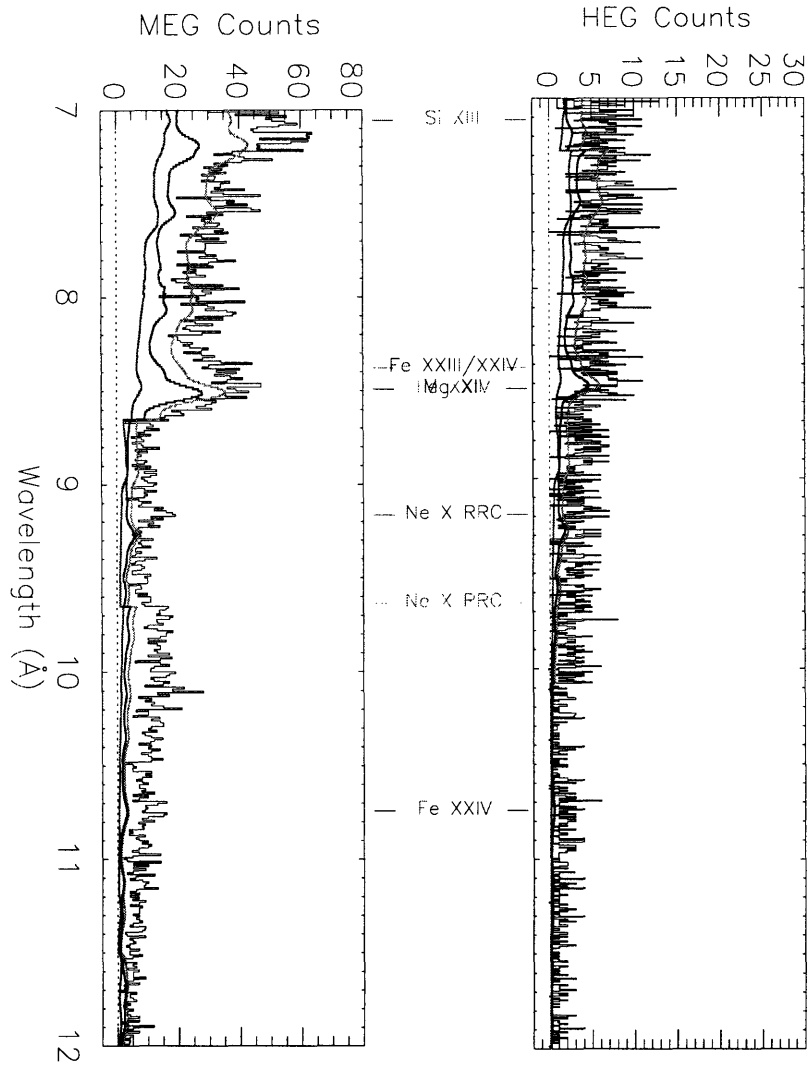

Figure 4-5: Same as Figure 4-3 except for the 7.0-12.0 Å region. As in Paper I, the overall model continuum is lower than the data in this wavelength range. Additionally, fewer emission features can be distinguished. The Ne X radiative recombination continuum (RRC) feature is observed in both jets. The RRC features are not predicted by the model, which assumes purely collisional ionization balance. There is excess emission near the red Si XIII line which can be attributed to a Si I fluorescence line that is not included in the plasma model.

at an angle α to the line of sight. Then, the Doppler shifts of the blue and red jets are given by

$$z = \gamma(1 \pm \beta\mu) - 1 \tag{4.1}$$

where $v_j = \beta c$ is the velocity of the jet flow,$\gamma = (1 - \beta^2)^{-1/2}$, and $\mu = \cos\alpha$. As in the first paper, high accuracy redshifts were used to obtain an estimate of the γ and β by adding the redshifts to cancel the $\beta\mu$ terms:

$$\gamma = \frac{z_b + z_r}{2} + 1 \tag{4.2}$$

giving $\beta = 0.2666 \pm 0.0006$. This value is slightly smaller than the β obtained in the first paper, 0.2699 ± 0.0007, and is closer to, but still larger than, the jet velocity determined by [17] based on the H-α lines. Substituting the value for β back into Eq. 4.1 and solving for α gives the angle of the jet to the line of sight during this observation: $\alpha = 84.6° \pm 0.1°$, which is within a few degrees of the expected angle.

All jet lines are clearly resolved. The line widths in Table 4.4 are consistent with the weighted average value (σ) of 1430 ± 167 km s^{-1}. Marginal evidence exists indicating a trend that the lower energy lines are slightly narrower than average. As found in Paper I, the widths in the red jet lines are consistent with those of the blue jet.

Consistent with Paper I results, the line widths are too large to result from thermal broadening for $kT < 10$ keV (see sec. 5) – 100-200 km s^{-1} – so the Doppler broadened widths must result from the divergence of a conical outflow [35]. Using the jet geometry in Figure 4-6, the maximum jet velocity, v_m, and the jet opening half angle, Θ, were determined: $v_m = 1940 \pm 227$ km s^{-1} and $\Theta = 1.35° \pm 0.16°$. This angle is about double the value found in Paper I due to wider lines from this observation. Similar to the first observation, the line widths are constant across the spectrum, indicating a single cone angle with $n_e \propto r^{-2}$.

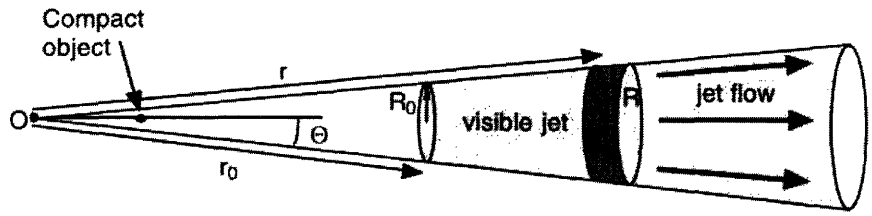

Figure 4-6: Geometry of a jet with uniform outflow (as taken from Paper I). Jet flow is radial, and observable quantities such as temperature are related to r, the distance from the cone's apex at O. The X-ray emitting portion of the jet is shaded, and its base is a distance r_o from the apex. The compact object is located on the jet axis some distance r_o from O.

Chapter 5

Modeling the Jet Emission Line Fluxes

To model the X-ray spectra, we use a plasma diagnostic approach where emission lines correspond to specific jet temperatures. In both the red and blue jets, we observe comparable line strengths in Fe, Ca, and Ar. Around 4 Å the red jet lines become weaker. Although Si and S are present in the red jet, these lines are not as strong as expected given the blue jet line fluxes. Therefore, we model the red jet with lower emission measures from the longer wavelength portions of the spectra.

As in Paper I, the spectra were modeled using `ISIS` and the APED atomic data base of line emissivities and ionization balance. The observed flux f_i of an emission line from a region with electron density n_e and temperature T is given by

$$f_i = \frac{J_i(T) \int n_e^2 dV}{4\pi D^2} = \frac{J_i(T) EM(T)}{4\pi D^2} \tag{5.1}$$

where $J_i(T)$ is the emissivity of a thin thermal plasma and $EM(T)$ is the emission measure of material with temperature T. For the geometry in Figure 4-6, temperature T varies with distance r, and we approximate Equation 5.1 by summing it over a discrete set of independent zones defined by $0.5r_j < r < 1.5r_j$:

$$f_i = \frac{\Omega \Sigma_j J_i(T_j) n_j^2 r_j^3}{4\pi D^2} \tag{5.2}$$

Zone	T (10^6 K)	Blue Jet EM (10^{57} cm^3)	Red Jet EM (10^{57} cm^3)	r (10^{10} cm)	n_e (10^{14} cm^{-3})
1	6.3	4.72	0	20.5	0.40
2	12.6	4.60	0	12.2	1.00
3	31.6	8.63	8.63	6.13	4.00
4	126.	8.83	8.83	2.17	20.0

Table 5.1: Jet Parameters from a Multi-Temperature Model. The interstellar absorption column density was fit simultaneously with the EM values at each temperature. The best fit absorption column was fixed at 2.07×10^{22} cm^{-2}. The values of r and n_e are derived using the adiabatically expanding jet model determined in Paper I.

where $\Omega = \pi\Theta^2$ and j indicates the component of the multitemperature model. Assuming approximately solar abundances, the emission measure distribution was estimated by fitting the line flux data with a four component model for both jets. A moderately good fit was obtained, as shown in Table 5.1. We assumed that the ISM absorption was the same as determined in Paper I: $N_H = (2.07 \pm 0.07) \times 10^{22}$ cm^{-2}. See Figs. 4-3 - 4-5 for a detailed comparison of the models with the HETGS data. No formal measurement of error bars is given, but based on Paper I, we anticipate they may be 30 percent bigger than those from the previous observation.

The abundances of Fe, S, Si, Mg, and Ne in the models for both jets were increased by 70% relative to H and He in order to reduce the model continuum to match the observed continuum. In Paper I, the abundances were increased 30% over the solar values. In the 8-12 Å region, the model predicts a continuum that is systematically low by up to a factor of 2. Adding a fifth temperature component, however, created emission lines that were not observed.

For the red jet, the same four temperature model was used as the blue jet. The two low temperature components were zeroed to model the low energy portion of the red jet as blocked by the companion due to eclipse. The resulting two temperature model is given in Table 5.1. This method produced reasonable agreement with the data except around the red jet Si XIII line.

Given the broader emission lines in this observation, the lack of Doppler boosting, and the slightly shorter exposure time compared to the first observation, the analysis

of the Si XIII did not produce stringent limits on the jet electron density. In the blue jet, the value of the ratio of the forbidden and intercombination lines, $R \equiv f/i = 1.79 \pm 0.70$, is consistent with the value determined in Paper I. However, it is also consistent with the asymptotic value as n_e drops below 10^{12} cm^{-3} for a plasma with $T = 5 \times 10^7$ K (where Si XIII is formed). The Si I fluorescence line is somewhat confused with the Si XIII of the red jet, making it difficult to compare its R or G values with those of the blue jet.

The spectrum is somewhat more complex than the model suggests: additional lines may be present at 8.1 Å and 10.1 Å that are not included in in the model, and the line at 5.1 Å (S XV in the blue jet) appears to be somewhat stronger in the model than the data. The Si XIII red jet line and the Fe XXIII/XIV blue jet line is much stronger than predicted by the model. The former occurrence may be attributed to emission from Si I fluorescence. Almost all the other line fluxes are explained to within 50% and the strongest lines are modelled to within 10%-20%. We consider the overall fit to be satisfactory.

It is clear from Fig. 4-3 that the highly ionized Fe lines are not occulted during the eclipse while lower ionization states of Si are not as strong in the receding jet (Fig. 4-4) as in the approaching jet. Thus the view of the system must be like that shown in Figs. 5-1 and 5-2, where the cooler parts of the jet suffer some occultation by the companion because they lie farther from the compact object than the hotter parts where the Fe lines are produced. Given that ions which exist in different temperature ranges have similar line widths and Doppler shifts, we assume that the flow has a constant opening angle and jet velocity (as in Paper I), with the result that the electron density n is proportional to r^{-2}.

Approximate values for the plasma parameters were determined iteratively in approximately fifty runs of the `ISIS` four-zone model. With a good model of the blue jet, the next step was to distinguish the differences in the red jet. To determine the range of acceptable emission measures for the red jet in the four-zone model, the emission measure of zone 1 was set to zero, and the second and third zone emission measures were varied in the model of the red jet as labelled in Table 3. Initially, the

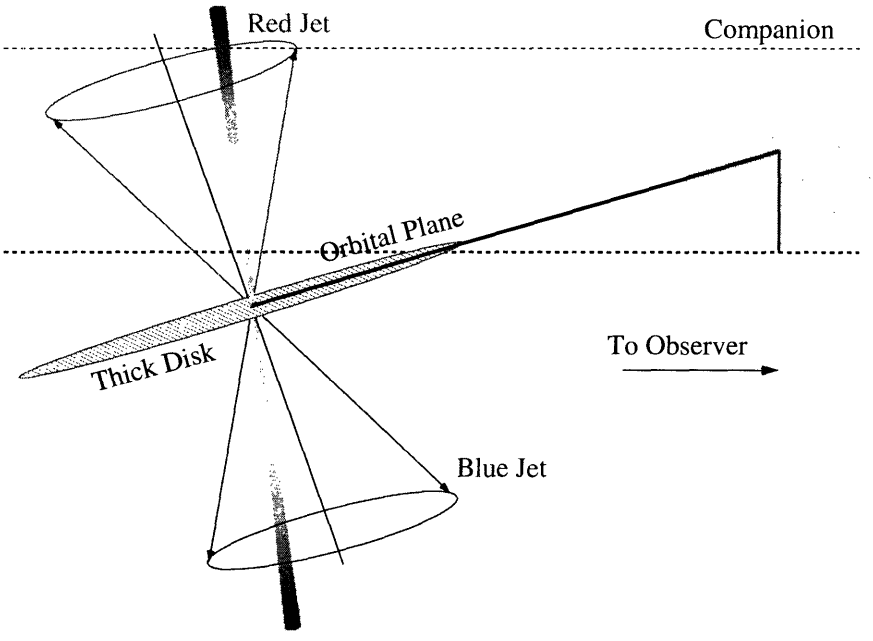

Figure 5-1: Schematic of the system geometry. During eclipse, the companion blocks the cool, outer portion of the red jet from the observer but not the hotter part that is closer to the compact object.

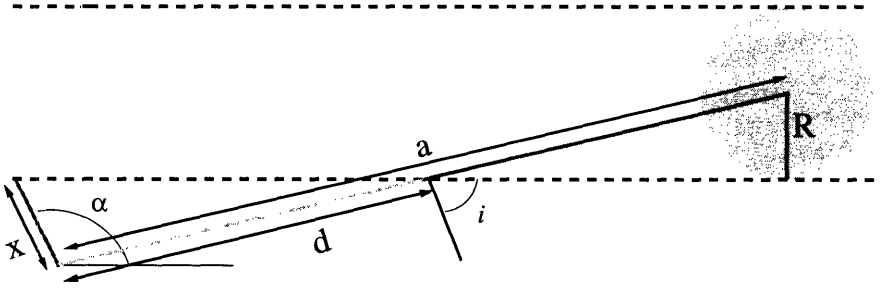

Figure 5-2: Geometry, as in Fig. 5-1, with distances and angles labeled. Appealing to basic trigonometry and geometry, we can use the measured value of x to find r, the radius of the companion. The angle α comes from (sec 4.3), the system inclination i comes from the standard kinematic model [17], and the semimajor axis a is derived from the system mass ratio and the size of the companion's Roche lobe (which may not be filled, see sec. 6.5). Thus, by measuring the distance x using fits to the X-ray spectrum, we can determine the length d and the stellar radius, R (sec. 6.5).

second and third component emission measures were zeroed, as displayed in Fig. 5-3. Then, the goodness of fits were tested for increasing values of the emission measures. Fig. 5-4 displays the fits used to determine the confidence limits on T_x.

Using $n \propto r^{-2}$ and the definition of emission measure, ζ is defined as the ratio of the emission measures of the occulted red and unocculted blue zones of the jet. If r_j is the radius of zone j, then ζ is related to x_j, the distance from the origin of the jet to the point of truncation in zone j, by

$$\zeta_j = \frac{EM_{red,j}}{EM_{blue,j}} = \frac{\int_{0.5r_j}^{x_j} n^2 dV}{\int_{0.5r_j}^{1.5r_j} n^2 dV} = \frac{\frac{1}{0.5r_j} - \frac{1}{x_j}}{\frac{1}{0.5r_j} - \frac{1}{1.5r_j}} = \frac{3}{2}(1 - \frac{r_j}{2x_j}) \tag{5.3}$$

where $r_j = 1.83 \times 10^{11}$ cm for the second zone ($j = 2$), and $r_j = 9.19 \times 10^{10}$ for the third zone ($j = 3$) in the jet model from Paper I (see table 5.1). Solving for x,

$$x_j = \frac{3r_j}{2}(3 - 2\zeta)^{-1}. \tag{5.4}$$

By visual inspection, we identify a range of reasonable models for the data. Using this method, we obtain a lower limit emission measure of 5.4×10^{57} cm^3 in the second zone and an upper limit of 1.16×10^{58} cm^3 in the third zone. The lower and upper limits to the truncation radius are then determined via eq. 5.4 to be 5.1×10^{10} cm and 8.5×10^{10} cm, respectively, so $x = (6.8 \pm 1.0) \times 10^{10}$ cm (for 1σ uncertainties).

Other conditions (besides eclipse) might cause the dimming observed in the cool portion of the red jet. For example, an electron scattering region could exist that linearly increases in optical depth with distance from the disk. Optical depth τ is related to jet length through the scattering region l by $\tau = \sigma_T n_e l \geq 1$, where σ_T is the Thomson scattering cross-section and n_e is the electron density. At the far side of the jet, $l = 2r\cos\alpha$, where r is the jet length 2×10^{11} cm and $\alpha = 84°$ from before. Therefore,

$$n_e \geq \frac{1}{2\sigma_T r \cos\alpha} \geq 3.6 \times 10^{13}\left(\frac{r}{2 \times 10^{11}}\right)^{-1} cm^{-3} \tag{5.5}$$

This result is very high and inconsistent with the observed densities. Thus, we

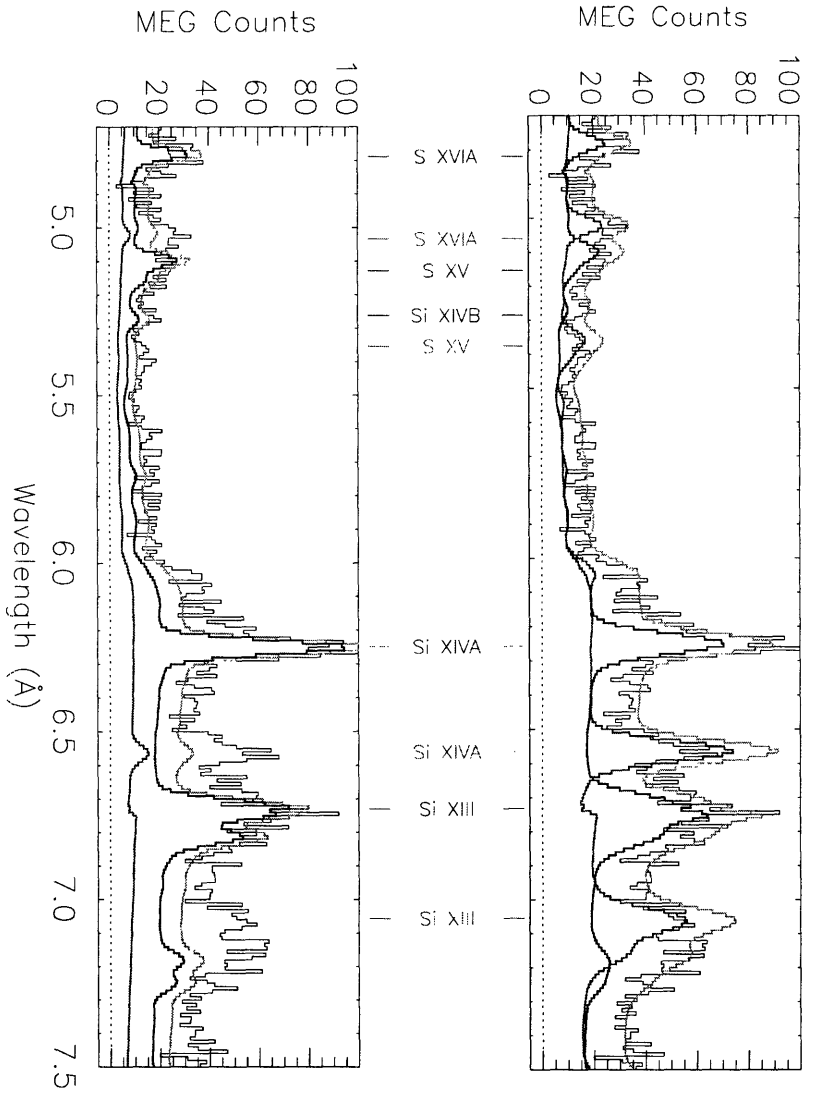

Figure 5-3: Examples of poor fits obtained by varying the emission measures of zones two and three (see Table 5.1) in the red jet model. The models are color-coded as in Figure 3. *Top:* Spectra and models using the same emission measures for zones two and three in the red jet model as in the blue jet model. The S XV, Si XIV, and Si XIII lines in the red jet are significantly overpredicted. *Bottom:* Same but with zeroed second and third emission measures in the red jet model. In this case, the S XV, Si XIV, Si XIII lines are almost nonexistent in the red jet model.

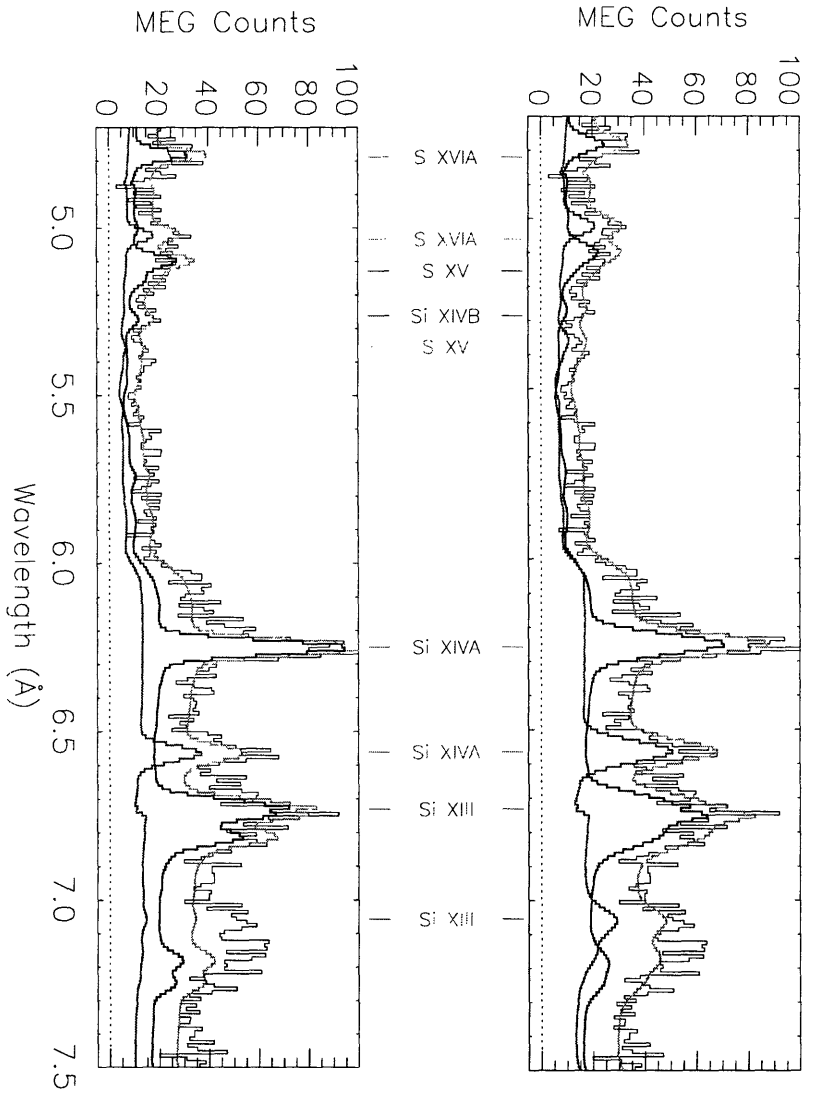

Figure 5-4: Same as the previous figure except plots with reasonable fits to the data. *Top:* Plot with the red jet zones one and two zeroed and with zone three 70% of the zone three blue jet value. Although slightly above the data, the Si XIV and Si XIII lines are reasonablely predicted by the model. This result gives a lower limit on the temperature at which the companion blocks the red jet. *Bottom:* Plot using 60% of the second component normalization of the blue jet model while zeroing the third component normalization. The model is a reasonable predictor for the observed lines (except around the Si fluorescence lines), and it places an upper limit on the temperature at which the companion blocks the red jet.

can discount the possibility of an electron scattering region far from the disk axis.

Chapter 6

Discussion

6.1 Relating the Jet to the Disk Corona

The opening half-angle from this observation is appoximately double the value from Paper I. In Paper I, we showed the jet opening half-angle Θ is consistent with the sound speed c_s at the base of the jet. We now explore the possibility that these two quantities are rigorously related. For a constant velocity jet with an expansion velocity, $v_m = c_s$, where c_s is the sound speed, the opening angle is given by

$$\tan\Theta = \frac{1}{\eta} = \frac{c_s}{v_j} \tag{6.1}$$

where η is the Mach number and v_j is the jet velocity, $0.2602c$.

For a nonrelativistic gas, the temperature at the base of the jet T_b is related to the jet speed and opening angle:

$$T_b = \frac{3\mu m_p(1+X)c_s^2}{5k} = \frac{3\mu m_p(1+X)v_j^2\tan^2\Theta}{5k} \tag{6.2}$$

where μ is the mean molecular weight of the plasma, and X is the ratio of the total ion density to the electron density, n_e. For the value $\Theta = 1.35°$ as observed, we find $T_b = (2.72 \pm 0.47) \times 10^8$ K. This value is almost triple the jet base temperature found in the first observation. This temperature corresponds to an energy of 23±4 keV, consistent with the results of [29] and others, who placed the jet-base energy at 30

keV.

The value of T_b is too large to be identified with the temperature in the disk, which would reach a maximum temperature of $\sim 10^7$ K at the innermost stable circular orbit about a 1 M black hole. The corona could have the right temperature and is where jets are thought to be launched [36]. If we ascribe the virial temperature of the disk corona to that at the base of the jet, then we may relate the jet base radius, R_b to T_b by

$$R_b = \frac{GM_1 m_e}{kT_b} \propto \frac{1}{\tan^2 \Theta} \tag{6.3}$$

where M_1 is the mass of the compact object and the proportionality comes from eq. 6.2. We infer from Eq. 6.3 and the $\times 2.3$ larger opening angle, that the jet is now launched $\times 5$ closer to the black hole than in the first observation. It seems likely, therefore, that the launch radius and, correspondingly, the jet base temperature, change episodically. Rewriting Eq. 6.3 in terms of the Schwarzschild radius, $R_s \equiv 2GM_1 c^{-2}$, then

$$R_b = \left(\frac{m_e c^2}{2kT_b}\right) R_s \tag{6.4}$$

where R_s is the Schwarzschild radius of the black hole. The jet launch radius R_b is 21.3 ± 3.1 R_s. Applying Eq. 6.4 to the first observation, the jet launch radius R_b was 104 ± 15 R_s. Figure 6-1 schematically represents the changes in the jets between observations. Both values are similar to what is found in simulations of magnetically confined jets [36].

6.2 Testing the Adiabatic Expansion Model

The thermal evolution of the jet depends on the relative dominance of two cooling terms: adiabatic expansion and radiative losses [29]. In the first HETGS observation, the emission measure distribution $EM(T)$ was adequately predicted from the adiabatic model. If adiabatic cooling dominates, then $T \propto r^{-4/3}$ for a nonrelativistic

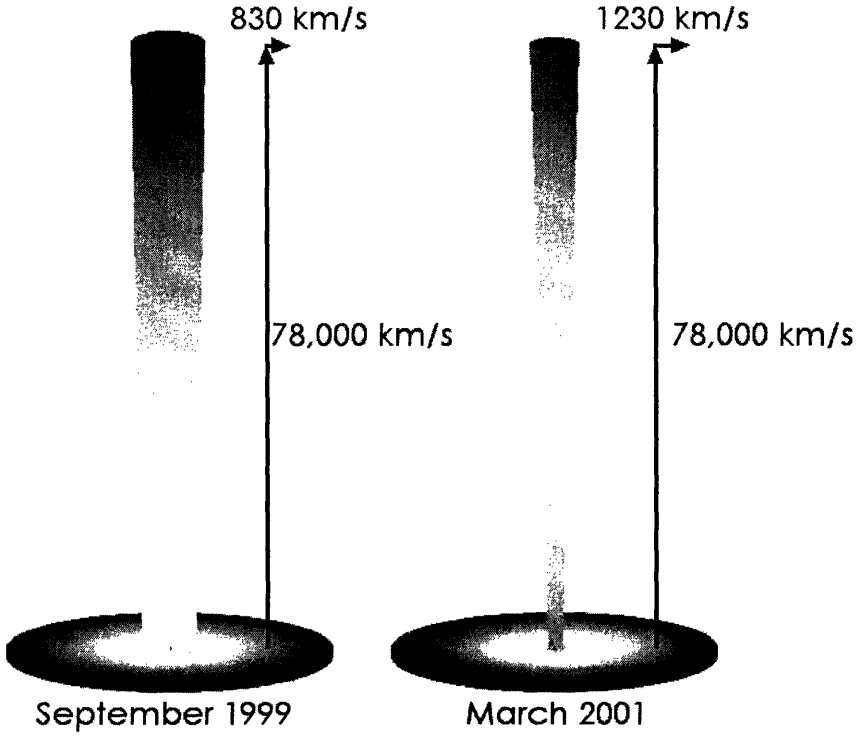

Figure 6-1: Schematic representation of the jet changes between the first and third HETGS observations. Emission line widths depend on the jet expansion velocity. Broader emission lines correspond to a higher expansion velocity that results from an increased temperature at the base of the jet. Applying these physical principles, a factor of two broader emission lines in the third observation corresponds to a jet launch radius five times closer to the compact object.

gas. Line profile measurements indicate the jet is a conical, uniform velocity flow (see Section 5), and $n_e n \propto r^{-4}$. Thus, $EM(T) \propto r^{-1} \propto T^{3/4}$. The agreement with this model is not perfect. Examination of Table 5.1 reveals the high temperature point is too low and the zone 1 emission measure is too high. The high temperature emission could be reduced by Comptonization in the highest density portion of the jet. The disagreement in the lowest temperature zone may be attributed to statistical uncertainties of order 30% (consistent with Paper I) from difficulty in detecting long wavelength lines. Here, we will explore other possible effects influencing the emission measure.

First, the metal abundances dominating line emission (Fe, S, Si, Mg) have changed from 1.3× solar to 1.7× solar between observations. If we assume a larger abundance, such as 2.0× solar and add a fifth spectral component, the continuum will increase dramatically overall. In this model, the component is thermal bremsstrahlung with sufficiently high temperature to strip detectable ions, $3 - 5 \times 10^8$ K. At high energy, the component would turn over spectrally, consistent with early estimates of the X-ray emission's peak temperature using *Ginga* [28, 37]. The plasma responsible for this X-ray emission, however, might originate from the disk corona rather than the jets.

Secondly, an estimate of the radiative cooling time scale at the base of the jet reveals it is substantially shorter than the flow time. From Paper I, we expect a cooling time, $t_r \equiv kT/(\Lambda[T]n_e) \sim 0.3$ s, whereas the flow time, $t_a \equiv r/v_j = 2.8$ s. With a rapid cooling time, the lower-temperature emission lines would be emitted in a small radial zone $t_r v_j \sim 2 \times 10^9$ cm thick, $\sim 10 - 100\times$ smaller than observed. To ameliorate this discrepancy, we consider that the jet may be filled with a "mist" of high-density clouds among lower-density plasma (known as a low filling factor, f). However, the density estimate from the Si XIII triplet remains valid as it samples the local density. Consequently, the predicted jet length would necessarily *increase* as $f^{-1/3}$ to obtain the observed line flux, and the cooling discrepancy becomes worse. Thus, a low-filling factor model does not yield better predictions of jet cooling time.

An improved model that may account for these dilemmas is one invoking substan-

tially higher abundances. For example, if the Si abundance is $\sim 10\times$ solar, the jet length decreases by $10^{1/3}$. From Paper I, we know resonance line trapping increases the optical depth to the cooling line radiation by a factor of 8, increasing the radiative cooling time due to resonance lines by a factor of 64. Thus, forbidden and intercombination lines, with small optical depths, dominate the cooling. These lines comprise less than 20% of the total line emission, so cooling time t_r reduces by a factor of ten after abundance effect considerations. Lacking a better model of the jet cooling, we assume the adiabatic model sufficiently describes the plasma cooling in the jets for the remainder of this thesis.

6.3 Fluorescence

We observed two unshifted line complexes likely due to fluorescence: one at 1.942±0.004 (Fe I-XII) and another at 7.131±006 (Si I-VII). The line fluxes are fairly substantial, with $1.\times10^4$ ph cm^{-2} s^{-1} for Fe and 0.3×10^4 ph cm^{-2} s^{-1} for Si, respectively. Adopting a distance of 4.85 kpc, the luminosities of these flourescence lines are on the order 10^{34} erg s^{-1}. This result is consistent with previous studies by [29] where Fe I was observed at comparable strength. Our observations cannot distinguish the source of the emission, whether from the accretion disk, a stellar wind, or the companion star. The deduced luminosities of the Si fluorescence complex are comparable to those observed in ionized stellar winds of HMXBs [38, 39, 40]. Future work is necessary to determine the origin of this fluorescence emission and any dependence on binary and precessional phase.

6.4 Determining the Unobscured Length of the Redward Jet

Without a direct estimate of the density in this observation, we now derive relations between the jet physical parameters and the observables in order to use the model from Paper I. To calculate the relative lengths of the jets for each observation, we

denote the September 1999 and March 2001 observations by the subscripts $i = 1$ and $i = 2$, respectively. The upper and lower limits on x were found in Section 5 used the model from Paper I to provide the radius of the second and third temperature zones where $r_{j1} = 1.22 \times 10^{11}$ cm for $j = 2$.

In the adiabatically expanding jet of nonrelativistic gas, the distance along the jet is asymptocally related to the temperature along it by

$$r_j = R_b \left(\frac{T_j}{T_b}\right)^{-3/4} = R_b \, T_j^{-3/4} \, T_b^{3/4} \tag{6.5}$$

[29]. For a given temperature zone, so $T_{j1} = T_{j2}$, we may relate the radius of that zone between observations where the electon temperature is not directly measured (as it was in Paper I) using eqs. 6.2 and 6.3, getting

$$\frac{r_{j1}}{r_{j2}} = \left(\frac{\tan \Theta_2}{\tan \Theta_1}\right)^{1/2} \approx \left(\frac{\Theta_2}{\Theta_1}\right)^{1/2}. \tag{6.6}$$

where Θ_i is the opening half angle for each observation.

Consequently, based on the ratio of opening angles inferred from the line widths (sec. 4.3), the jet scale length is approximately one and half times larger than in the first observation. Given the visible jet length computed in Sec. 6.4 on the basis of the jet scale length inferred from the first observation, we find $x_{j2} = (1.02 \pm 0.15) \times 10^{11}$ cm for this observation.

6.5 Inferring the Binary Geometry and Black Hole Mass

We assume the system has the geometry shown in Fig. 5-1 and approximate that the companion fully eclipses the receding jet. Then, using the angles intrinsic to the system in Fig. 5-2, d, the distance from the source of the jets to the point of intersection of the line of sight and the orbital plane, can be calculated:

$$d = \frac{x \sin \alpha}{\sin(90 - i)} \tag{6.7}$$

With x_{j2} from sec. 6.4, $d = (5.2 \pm .8) \times 10^{11}$ cm. For a circular orbit, semimajor axis a can be determined from the observable quantities K_x and K_o, the semiamplitude velocities of the compact object and companion, respectively:

$$a = \frac{P(K_x + K_o)}{2\pi \sin i} = \frac{PK_x(1+q)}{2\pi \sin i} \tag{6.8}$$

where $q \equiv \frac{M_x}{M_o} = \frac{K_o}{K_x}$, and M_x and M_o are the masses of the compact object and companion, respectively. With K_x= 175±20 km s^{-1} [41] and K_o = 100±15 km s^{-1} [20], $a = (3.8 \pm 0.4) \times 10^{12}$ cm.

Using the geometry shown in Figure 5-2, the radius R of the companion is related to a, d, and i:

$$R = (a - d) \cos i. \tag{6.9}$$

With $i = 78.83°$ from the kinematic model margon89, we find $R = (6.3 \pm 0.7) \times 10^{11}$ cm, or $(9.1 \pm 1.0) R_{sun}$. The uncertainty in the estimated radius is dominated by the uncertainty in the semimajor axis because d and its uncertainty are rather small compared to a. The value of R is approximately one-third of the Roche volume radius. Therefore, the companion does not fill the Roche lobe, and accretion probably occurs through stellar wind as might be expected from an early type star.

Given the small radius of the companion, we will assume it is a main sequence star. Consequently, we can estimate its mass based on its radius. A radius of $9.1 R_{sun}$ corresponds to a mass of 29 ± 7 M_{sun} for an 08 spectral class star, consistent with wind accretion. Using K_x and K_o from before, we find that the mass of the compact object is 16 ± 4 M_{sun}. This argument indicates the compact object responsible for the relativistic jets is a black hole.

Previous work (for example, [42]) argues the SS 433 companion must fill its Roche lobe radius R_L. To check the consistency of this conclusion with our result, we note that semimajor axis a is related to R_L:

$$a = R_L(1+q)^{1/2}. \tag{6.10}$$

If $R = R_L = (9.1 \pm 1.0)R_{sun}$ and $K_o/K_x = 0.57 \pm 0.11$ from above, $a = (1.11 \pm 0.2) \times 10^{12}$ cm. Solving Eq. 6.9 for d, we find

$$d = \frac{a\cos i - R_L}{\cos i} \tag{6.11}$$

With $i = 78.83°$, we obtain a negative value for d. Thus, the companion cannot be Roche lobe filling in our model.

Chapter 7

Conclusion

Despite twenty-five years of study, SS 433 remains an enigmatic astrophysical source. We observed SS 433 with *Chandra*, the most sophisticated X-ray telescope to date, in an attempt to reveal the conditions and nature of this mysterious system. Using the HETGS, we obtained high-resolution X-ray spectra from the jets of SS 433 during various precessional and orbital phases. Through physical modeling of this data, we have probed close to the compact object and observed changes in the jet bases. Additionally, analysis of spectra during eclipse facilitated estimates of the compact object and donor star sizes, vital information to elucidating the evolutionary status, accretion mechanisms, and origins of precession.

This work generates numerous issues to be addressed in future studies of SS 433, both observational as well as theoretical. Foremost, the efficacy of the adiabatic model should be examined through further X-ray spectroscopy. Resolved optical measurements are needed in order to determine K_o and K_x more definitevely as a means to concretely coclude the nature of the binary. Work is also necessary to assess how and why the jet launch base changes over time.

Motivated by the work in this thesis, we have recently been awarded 200 ks of *Chandra* HETGS time for next year. We will pursue simultaneous X-ray, optical, and radio observations as a means to examine the jets and their changes as they move outward. Additionally, we have submitted scientific proposals to use the Magellan Observatory for high resolution optical spectroscopy to study the disk and companion

in SS 433. Ultimately, we plan to continue research on SS 433 as a means to better understand, refine, and apply the laws of physics to astronomical systems.

Bibliography

[1] Giacconi, R. et al. 1962 Physical Review Letters, 9, 439

[2] Bradt, H., Ohashi, T., & Pounds, K. A. 1992, Astronomy & Astrophysics, 30, 391

[3] Charles, P. A., & Seward, F. D. 1995, Exploring the X-ray Universe, Cambridge University Press, Cambridge, UK

[4] Forman, W., Schwarz, J., Jones, C., Liller, W., Fabian, A. 1979, Astrophysical Journal Letters, 234, L27

[5] Tananbaum, H., Gursky, H., Kellogg, E., Levinson, R., Schreier, E., & Giacconi, R. 1972 Astrophysical Journal Letters, 174, L143

[6] Schreier, E., Gorenstein, P., & Feigelson, E., 1982, Astrophysical Journal, 261, 42

[7] Allen's Astrophysical Quantities Fourth Edition, ed. Cox. 2000, AIP Press, New York

[8] Van Der Kils, M. 1989 Annual Review of Astronomy & Astrophysics, 27, 517

[9] Kitamoto, S., Tsunemi, H., Miyamoto, S., Yamashita, K., & Mizobuchi, S., et al. 1989, Nature, 342, 518

[10] Gurskey, H. 1966 Astrophysical Journal, 146, 310

[11] Sandage, A. R. 1966, Astrophysical Journal, 146, 315

[12] Gottlieb, E. W., Wright, E. L., & Liller, W. 1975, Astrophysical Journal Letters, 195, L33

[13] Stephenson, C. B. & Sanduleak, N. 1977, Astrophysical Journal Supplement, 33, 459

[14] Fabian, A. C. & Rees, M. J. 1979, MNRAS, 187, 13

[15] Milgrom, M. 1979, Astronomy & Astrophysics, 76, L3

[16] Abell, G. O. & Margon, B. 1979, Nature, 279, 701

[17] Margon, B. & Anderson, S. F. 1989, Astrophysical Journal, 347, 448

[18] Crampton, D., Cowley, A. P., & Hutchings, J. B. 1980, Astrophysical Journal Letters, 235, L131

[19] Crampton, D. & Hutchings, J. B. 1981, Astrophysical Journal, 251, 604

[20] Gies et al. 2002, Astrophysical Journal, 566, 1069

[21] Gies, D. R., Huang, W., & McSwain, M. V. 2002, Astrophysical Journal Letters, 578, L67

[22] Hillwig, T. et al. 004, Astrophysical Journal, submitted

[23] Hjellming, R. & Johnston, S. 1981, Astrophysical Journal, 246, L141

[24] Vermeulen, R. C., Schilizzi, R. T., Spencer, R. E., Romney, J. D., & Fejes, I. 1993, Astronomy & Astrophysics, 270, 177

[25] Davidson & McCray, 1980, Astrophysical Journal, 240, 1082

[26] Watson, M. G., Willingale, R., Grindlay, J. E., & Seward, F. D. 1983, Astrophysical Journal, 273, 688

[27] Marshall, F. E., Swank, J. H., Boldt, E. A., Holt, S. S., & Serlemitsos, P. J. 1979, Astrophysical Journal, 230, 145

[28] Brinkmann, W., Kawai, N., Matsuoka, M., & Fink, H. H. 1991, Astronomy & Astrophysics, 241, 112

[29] Kotani, T., Kawai, N., Matsuoka, M, & Brinkmann, W. 1996, PASJ, 48, 619

[30] Marshall, H. L., Canizares, C. R., & Schulz, N. S. 2002, Astrophysical Journal, 564, 941

[31] Kotani et al. 1994, PASJ, 46, L1

[32] Stewart, G. C., Watson, M. G., Matsuoka, M., Brinkmann, W., Jugaku, J., Takagishi, K., Omodaka, T., Kemp, J. C., Kenson, G. D., Kraus, D. J., Mazeh, T., and Leibowitz, E. M. MNRAS, 228

[33] Gladyshev, S. A., Goranskii, V. P., & Cherepashchuk, A. M., 1987, Soviet Astronomy, 31 541

[34] Fender, F., Migliari, S., & Mendez, M. 2003, New Astronomy Reviews, 47, 6

[35] Begelman, M. C., Sarazin, C. L., Hatchett, S. P., McKee, C. F., & Arons, J. 1980, Astrophysical Journal, 238, 722

[36] Meier, D. L., Koide, S. & Uchida, Y. 2001, Science, 291, 84

[37] Yuan, W., Kawai, N., Brinkmann, W., & Matsuoka, M. 1995, Astronomy & Astrophysics, 297, 451

[38] Schulz, N. S., Canizares, C. R., Lee, J. C., & Sako, M. 2002, Astrophysical Journal, 564, L21

[39] Wojdowski, P. S., Liedahl, D. A., Sako, M., Kahn, S. M., & Paerels, F., 2003, Astrophysical Journal, 582, 959

[40] Boroson, B., Vrtilek, S. D., Kallman, T., & Corcoran, M., 2003, Astrophysical Journal, 592, 516

[41] Fabrika, S. N. & Bychkova, L. V. 1990, Astronomy & Astrophysics, 240, L5.

[42] King, A. R., Taam, R. E., Begelman, M. C., 2000, Astrophysical Journal Letters, 530, L25